Prediction of transonic Aerodynamic Forces via nonlinear reduced-order models

Zhijun Yang*, Rui Huang*, Yonghui Zhao*, Haiyan Hu*
**State Key Laboratory of Mechanics and Control of Mechanical Structures,*
Nanjing University of Aeronautics and Astronautics,
210016 Nanjing, People's Republic of China

Summary. In this paper, the transonic aerodynamic forces are investigated via a novel nonlinear reduced-order model. The reduced-order model was represented by a nonlinear Wiener-Hammerstein models, and the corresponding parameters were estimated using a nonlinear system identification scheme. Based on the present nonlinear reduced-order model of transonic aerodynamic systems, transonic aeroelastic models can be established to predict the aeroelastic behaviors. To demonstrate the accuracy of these nonlinear models, the comparison of transonic aerodynamic force and flutter boundary computed via CFD and ROM of the three-dimensional Benchmark Active Control Technology (BACT) wing was first investigated.

1. Introduction

As well known, the nonlinear aerodynamic forces computed via the code of Computational Fluid Dynamics (CFD) are most reliable, but the large amount of computation makes it difficult to apply CFD to active flutter suppression. To solve this problem, great efforts have been made to establish Reduced-Order Models (ROMs), instead of high-dimensional model of CFD, to compute the nonlinear aerodynamic forces. As summarized by Rozza [1], ROM has had a great variety of mathematical forms. The major methods of order reduction can be divided into three categories. The first uses subspace projection techniques, such as the Proper Orthogonal Decomposition [2-3] and harmonic balance, the second adopts generalized interpolation methods, such as Radial Basis Functions or Kriging interpolators [4-5], and the third uses identification techniques based on the input-output data, such as Volterra theory and neural networks [6-7]. Although ROMs have witnessed successful applications to many engineering fields, some problems are still open in aeroelastic dynamics. The most essential problem is the ability to accurately model important aeroelastic phenomena, such as Limit Cycle Oscillations (LCOs).

In this study, a parallel ROM of Wiener-Hammerstein type is proposed for modeling nonlinear aerodynamic systems. In Section 2, the method for establishing a nonlinear ROM of transonic aerodynamic systems is presented. In Section 3, the ROM for an aeroservoelastic problem of a three-dimensional Benchmark Active Control Technology (BACT) wing is established. In Section 4, a discussion is made for the numerical simulations implemented to verify the accuracy of the nonlinear ROM and finally, a few concluding remarks are made in Section 5.

2. Parallel Reduced-Order Model of Wiener-Hammerstein Type

The Wiener model comprises a front linear part and a rear nonlinear part, and the Hammerstein model comprises a front nonlinear part and a rear linear part. Both models are able to describe nonlinear systems properly. The Wiener-Hammerstein model, developed via the Wiener and Hammerstein models, consists of a front linear part, a middle nonlinear part and a rear linear part so that it has stronger ability to simulate nonlinear systems. Huang et al. presented a parallel ROM of Wiener type to efficiently estimate the dynamic pressure and oscillation frequency of the BACT wing in a flutter [8]. Their numerical results showed that the parallel ROM of Wiener type was able to accurately predict the transonic flutter boundary, but failed to accurately simulate the nonlinear aeroelastic behaviors, such as a limit-cycle oscillation. In this section, a novel nonlinear ROM approach is presented.

2.1 Structure of Parallel ROM of Wiener-Hammerstein Type

As shown in Fig.1, the single-layer ROM of Wiener-Hammerstein type yields

$$\begin{aligned} \boldsymbol{x}_w(k+1) &= \boldsymbol{A}_w \boldsymbol{x}_w(k) + \boldsymbol{B}_w \boldsymbol{u}(k), \\ \boldsymbol{y}(k) &= \boldsymbol{C}_w \boldsymbol{x}_w(k) + \boldsymbol{D}_w \boldsymbol{u}(k), \end{aligned} \tag{1}$$

$$\boldsymbol{y}'(k) = f\left(\boldsymbol{y}(k)\right), \tag{2}$$

$$\begin{aligned} \boldsymbol{x}_h(k+1) &= \boldsymbol{A}_h \boldsymbol{x}_h(k) + \boldsymbol{B}_h \boldsymbol{y}'(k), \\ \tilde{\boldsymbol{y}}'(k) &= \boldsymbol{C}_h \boldsymbol{x}_h(k) + \boldsymbol{D}_h \boldsymbol{x}_h(k), \end{aligned} \tag{3}$$

where $\boldsymbol{x}_w \in \Re^p$, $\boldsymbol{x}_h \in \Re^q$, $\boldsymbol{u} \in \Re^m$, $\boldsymbol{y} \in \Re^n$, $\boldsymbol{y}' \in \Re^n$ and $\tilde{\boldsymbol{y}}' \in \Re^n$ are the state vector of the front linear part, the state vector of the rear linear part, the input vector and output vector of the front linear part, the output vector of the middle nonlinear part, and the output vector of the rear linear part, respectively. $\boldsymbol{A}_w \in \Re^{p\times p}$, $\boldsymbol{B}_w \in \Re^{p\times m}$, $\boldsymbol{C}_w \in \Re^{n\times p}$, $\boldsymbol{D}_w \in \Re^{n\times m}$, $\boldsymbol{A}_h \in \Re^{q\times q}$, $\boldsymbol{y}'(k) = f\left(\boldsymbol{y}(k)\right)$ $\boldsymbol{B}_h \in \Re^{q\times n}$, $\boldsymbol{C}_h \in \Re^{n\times q}$ and $\boldsymbol{D}_h \in \Re^{n\times n}$ are the system matrix, input matrix, output matrix, and the direct feed through the matrices of the front linear part and the rear linear part, respectively. $f(\bullet)$ is a smooth, static, nonlinear function.

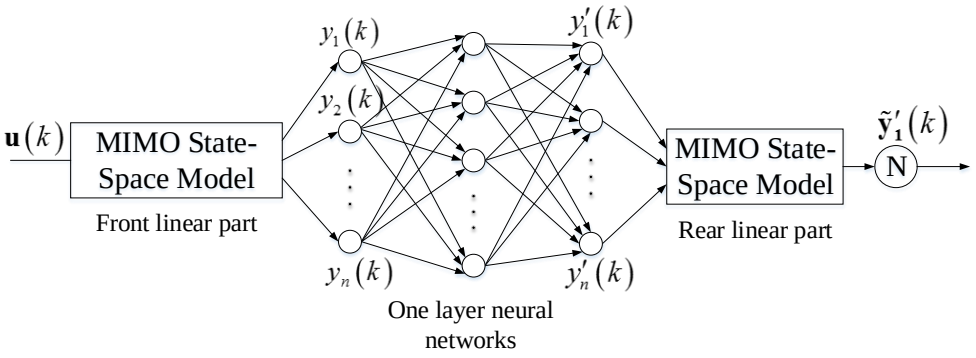

Fig.1 One layer ROM of Wiener-Hammerstein type

Fig.2 shows the parallel ROM structure, where $\boldsymbol{u}(k)$ is the input of the front linear part for the time instant k. The front linear part can use the transfer function, the state space function or other linear functions, and the rear linear part is the same. The middle nonlinear part can use a variety of functions, such as piecewise nonlinear functions, saturation functions, and neural networks. $\tilde{\boldsymbol{y}}_i'(k), i = 1, 2 \ldots z$ is the output of the rear linear part, which estimates the generalized aerodynamic force.

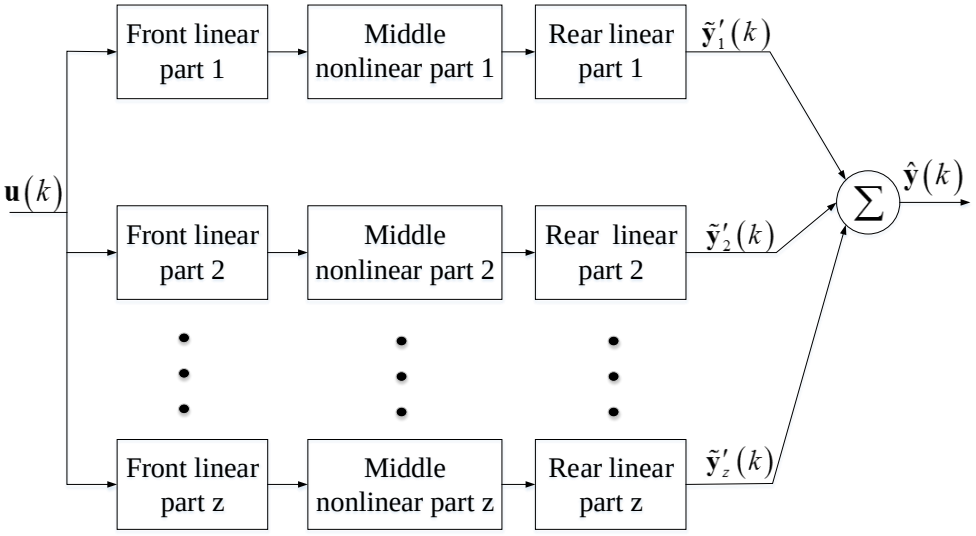

Fig.2 Parallel ROM of Wiener-Hammerstein type for aerodynamic system

In this study, the first layer of the ROM is first identified from the input and output data of CFD. Then, the input data of CFD and the difference between the output data of CFD and those of the first layer are used as the input and output data, respectively, to identify the second layer. This procedure can be repeated until the generalized aerodynamic forces predicted by ROM satisfy the given accuracy. As a symbol of the end of the cycle, the percentage of the coefficient of Variance Accounted For (VAF) between the output data of CFD and those estimated is defined as follows

$$vaf = \max\left(1 - \frac{\mathrm{var}\left(y_{rel} - y_{pre}\right)}{\mathrm{var}\left(y_{rel}\right)}, 0\right). \tag{4}$$

The VAF value decreases as an increase of the signal differences. The VAF is 100% when the two signals are completely consistent. When a new layer of the ROM is identified, the VAF value between the real output data and those estimated is computed. The above cycle stops when the VAF value is less than 5% because the layer has almost no useful information. If this is case, the layer should not be added into the parallel ROM layer. When all of the layers of the parallel ROM are identified, the final output of the parallel ROM can be computed as

$$vaf = \max\left(1 - \frac{\mathrm{var}\left(y_{rel} - y_{pre}\right)}{\mathrm{var}\left(y_{rel}\right)}, 0\right). \tag{5}$$

2.2 Identification of Front Linear Part of Parallel ROM of Wiener-Hammerstein Type

As studied by Huang et al. [8-9], the linear part identified by using the optimized Predictor-Based Subspace Identification (PBSID) method [10-11] has many advantages, such as high precision and strong stability, and can be

applied to the closed loop system. In addition, once the input and output data of the CFD are obtained, the linear part can be uniquely determined via optimized PBSID.
First, a Vector AutoRegressive with eXogenous inputs (VARX) predictor can be described as

$$\boldsymbol{y}(k)=\sum_{i=0}^{t}\boldsymbol{B}_i\boldsymbol{u}(k-i)+\sum_{i=1}^{t}\boldsymbol{A}_i\boldsymbol{y}(k-i), \tag{6}$$

where $k\in\mathbb{N}^+$ is the size of the past window, $\boldsymbol{A}_i$ and $\boldsymbol{B}_i$ are the matrices to be estimated. To simplify the identification, the matrix $\boldsymbol{\Theta}\in\mathbb{R}^{n\times(m(t+1)+nt)}$ that contains $\boldsymbol{A}_i$ and $\boldsymbol{B}_i$ becomes the only VARX parameter to be identified and is denoted as

$$\boldsymbol{\Theta}\triangleq\begin{bmatrix}\boldsymbol{B}_t & \boldsymbol{B}_{t-1} & \cdots & \boldsymbol{B}_0 & \boldsymbol{A}_t & \boldsymbol{A}_{t-1} & \cdots & \boldsymbol{A}_1\end{bmatrix}. \tag{7}$$

The VARX parameters can be identified by the least squares method as

$$\boldsymbol{\Theta}=\boldsymbol{Y}\boldsymbol{\Omega}^{+}, \tag{8}$$

where $(\bullet)^{+}$ is the pseudo inverse and $\boldsymbol{Y}$ and $\boldsymbol{\Omega}$ is denoted as

$$\boldsymbol{Y}\triangleq\begin{bmatrix}\boldsymbol{y}_{t+1} & \boldsymbol{y}_{t+2} & \cdots & \boldsymbol{y}_{N-1} & \boldsymbol{y}_N\end{bmatrix}, \tag{9}$$

$$\boldsymbol{\Omega}\triangleq\begin{bmatrix}\boldsymbol{u}_1 & \boldsymbol{u}_2 & \cdots & \boldsymbol{u}_{N-t}\\ \boldsymbol{u}_2 & \boldsymbol{u}_3 & \cdots & \boldsymbol{u}_{N-t+1}\\ \vdots & \vdots & \ddots & \vdots\\ \boldsymbol{u}_{t+1} & \boldsymbol{u}_{t+2} & \cdots & \boldsymbol{u}_N\\ \boldsymbol{y}_1 & \boldsymbol{y}_2 & \cdots & \boldsymbol{y}_{N-t}\\ \boldsymbol{y}_2 & \boldsymbol{y}_3 & \cdots & \boldsymbol{y}_{N-t+1}\\ \vdots & \vdots & \ddots & \vdots\\ \boldsymbol{y}_t & \boldsymbol{y}_{t+1} & \cdots & \boldsymbol{y}_{N-1}\end{bmatrix}. \tag{10}$$

Once the AVRX parameters are defined, the system matrices $\boldsymbol{A}_w,\boldsymbol{B}_w,\boldsymbol{C}_w,\boldsymbol{D}_w$ in Eq.(11) can be identified via the subspace identification method. The details of the identification process can be found in Chiuso [10] and Houtzager et al. [12]. The system matrices can be obtained as

$$\begin{aligned}\begin{bmatrix}\boldsymbol{A}_w & \boldsymbol{B}_w\end{bmatrix}&=\bar{\boldsymbol{X}}_{(:,2:N-t)}\begin{bmatrix}\bar{\boldsymbol{X}}_{(:,1:N-t-1)}\\ \boldsymbol{U}_{(:,1:N-t-1)}\end{bmatrix}^{+},\\ \begin{bmatrix}\boldsymbol{C}_w & \boldsymbol{D}_w\end{bmatrix}&=\boldsymbol{Y}_{(:,1:N-t-1)}\begin{bmatrix}\bar{\boldsymbol{X}}_{(:,1:N-t-1)}\\ \boldsymbol{U}_{(:,1:N-t-1)}\end{bmatrix}^{+},\end{aligned} \tag{12}$$

where the input vector $\boldsymbol{U}$ is denoted the same form as $\boldsymbol{Y}$.

2.3 Identification of Nonlinear Part of Parallel ROM of Wiener-Hammerstein Type

As stated above, the linear part identified via the PBSID method with the CFD input and output data can be used as the initial parameters of the front linear part. As well known, neural networks serve as an excellent method to describe nonlinear systems. In this study, hence, a neural network is used as the nonlinear part, where the neural network is composed of z neurons described by $\tanh$. The parameters of the nonlinear part are identified via the Levenberg-Marquadt (LM) [13] algorithm and then optimized with the initial parameters of the front linear part all together by the LM algorithm again. The second optimization may change the initial parameters to reach the goodness fit of the CFD output and parallel ROM output data.

2.4 Identification of Rear Linear Part of Parallel ROM of Wiener-Hammerstein Type

Once the parameters of the front linear part and the nonlinear part are determined, the subsequent step is to determine the parameters of the rear linear part. This procedure can be completed by using the output of the nonlinear part and the CFD output as the input and output data via the PBSID algorithm. When layer ith of the parallel ROM is estimated, the residuals of the output are computed as

$$\boldsymbol{y}_{res}(k)=\boldsymbol{y}_{rel}(k)-\sum_{j=1}^{i}\tilde{\boldsymbol{y}}_j'(k), \tag{13}$$

where $\boldsymbol{y}_{res}(k)$ is the output residuals and used as the output of the next layer. If the VAF value of the (i+1)th layer computed via Eq. (14) is less than 5%, the new layer most likely does not contain useful information and, therefore, the parallel ROM is made up of the front i Wiener-Hammerstein models.

3 Dynamic Equation of Aeroservoelastic System

This section presents the aeroservoelastic model of the BACT wing via the parallel ROM. A BACT wing equipped with a trailing-edge control surface and upper- and lower-surface spoilers has been widely studied in numerical simulations and experiments [14-15]. In this study, the BACT wing with a trailing-edge control surface only is used to verify the accuracy of the parallel ROM.

The dynamic equation of the BACT wing with a trailing-edge control surface yields

$$\begin{aligned}&\begin{bmatrix} M & S_\alpha \\ S_\alpha & I_\alpha \end{bmatrix}\begin{Bmatrix} \ddot{h} \\ \ddot{\alpha} \end{Bmatrix}+\begin{bmatrix} 2M\zeta_h\omega_h & 0 \\ 0 & 2I_\alpha\zeta_\alpha\omega_\alpha \end{bmatrix}\begin{Bmatrix} \dot{h} \\ \dot{\alpha} \end{Bmatrix}+\begin{bmatrix} K_h & 0 \\ 0 & K_\alpha \end{bmatrix}\begin{Bmatrix} h \\ \alpha \end{Bmatrix}\\ &=-\begin{Bmatrix} S_\beta \\ S_{\alpha\beta} \end{Bmatrix}\ddot{\beta}+q_\infty\begin{Bmatrix} Q_h \\ Q_\alpha \end{Bmatrix},\end{aligned} \tag{15}$$

where h, α, and β are the plunge displacement, the pitch angle of the BACT wing and the deflection angle of the trailing-edge control surface, respectively. q_∞ is the dynamic pressure of coming flow, Q_h and Q_α are the unsteady lift force and moment, respectively. In the study, the parameters of the BACT wing are taken as

$$\begin{aligned}&M = 6.08 \text{ slug}, \quad S_a = 0.0142 \text{ slug-ft},\\ &S_\beta = 0.00288 \text{ slug-ft}, \quad I_\alpha = 2.80 \text{ slug-ft}^2,\\ &\omega_h = 21.01 \text{ rad/s}, \zeta_h = 0.0014, \omega_\alpha = 32.72 \text{ rad/s},\\ &\zeta_\alpha = 0.001, \quad S_{\alpha\beta} = 0.00157 \text{ slug-ft}^2,\\ &K_h = 2686 \text{ lb/ft}, \quad K_\alpha = 3000 \text{ ft-lb}.\end{aligned} \tag{16}$$

The physical explanations of above parameters can be found in Waszak et al. [16].

The equation (17) can be recast in the modal space

$$\begin{aligned}&\begin{bmatrix} 1 & 0 \\ 0 & 1 \end{bmatrix}\begin{Bmatrix} \ddot{\xi}_1 \\ \ddot{\xi}_2 \end{Bmatrix}+\begin{bmatrix} 2\zeta_h\omega_h & 0 \\ 0 & 2\zeta_\alpha\omega_\alpha \end{bmatrix}\begin{Bmatrix} \dot{\xi}_1 \\ \dot{\xi}_2 \end{Bmatrix}+\begin{bmatrix} \omega_h^2 & 0 \\ 0 & \omega_\alpha^2 \end{bmatrix}\begin{Bmatrix} \xi_1 \\ \xi_2 \end{Bmatrix}\\ &=-\boldsymbol{\phi}^T\begin{Bmatrix} S_\beta \\ S_{\alpha\beta} \end{Bmatrix}\ddot{\beta}+q_\infty\boldsymbol{\phi}^T\begin{Bmatrix} Q_h \\ Q_\alpha \end{Bmatrix},\end{aligned} \tag{18}$$

where $\boldsymbol{\phi}$ is the mode shape matrix, ξ_1 and ξ_2 are the modal displacements of the first order and the second order, respectively. In practice, the deflection angle of the control surface cannot respond instantaneously to the control input, but yields the following dynamic model of the actuator

$$\ddot{\beta}+2\omega_0\zeta\dot{\beta}+\omega_0^2\beta=k_0\omega_0^2\beta_c, \tag{19}$$

where k_0, ζ, ω_0, and β_c are the gain, the damping coefficient, the natural frequency and the control command, respectively. The values of these parameters and their physical explanations have been discussed by Waszak et al. [16] in detail. Eventually, the aeroservoelastic equation of the BACT wing with the dynamic model of actuator is formulated as

$$\dot{\boldsymbol{x}}_s = \boldsymbol{A}_s\boldsymbol{x}_s + \boldsymbol{B}_c\beta_c + q_\infty\boldsymbol{B}_q\boldsymbol{Q}, \tag{20}$$

where $\boldsymbol{x}_s=\begin{bmatrix} \xi_1 & \xi_2 & \beta & \dot{\xi}_1 & \dot{\xi}_2 & \dot{\beta} \end{bmatrix}^T$ is the state variable vector, and the definitions of matrices $\boldsymbol{A}_s$, $\boldsymbol{B}_c$, $\boldsymbol{B}_q$, and $\boldsymbol{Q}$ can be found in Appendix C.

$$\begin{aligned}&\boldsymbol{A}_s=\begin{bmatrix} \boldsymbol{0}_{3\times3} & \boldsymbol{I}_3 \\ -\boldsymbol{M}^{-1}\boldsymbol{K} & -\boldsymbol{M}^{-1}\boldsymbol{C} \end{bmatrix}, \boldsymbol{B}_c=\begin{bmatrix} \boldsymbol{0}_{3\times1} \\ -\boldsymbol{M}^{-1}\tilde{\boldsymbol{B}} \end{bmatrix},\\ &\boldsymbol{B}_q=\begin{bmatrix} \boldsymbol{0}_{3\times2} \\ \boldsymbol{M}^{-1}[\boldsymbol{I}_2;\boldsymbol{0}_{1\times2}] \end{bmatrix}, \boldsymbol{Q}=\begin{bmatrix} Q_h \\ Q_\alpha \end{bmatrix},\end{aligned} \tag{21}$$

where

$$\boldsymbol{M}=\begin{bmatrix}1&0&0\\0&1&0\\0&0&1\end{bmatrix},\ \boldsymbol{C}=\begin{bmatrix}2\zeta_1\omega_1&0&-2\omega_\beta\zeta_\beta M_{\xi_1\beta}\\0&2\zeta_2\omega_2&-2\omega_\beta\zeta_\beta M_{\xi_2\beta}\\0&0&2\zeta_\beta\omega_\beta\end{bmatrix},$$
$$\boldsymbol{K}=\begin{bmatrix}\omega_1^2&0&-\omega_\beta^2 M_{\xi_1\beta}\\0&\omega_2^2&-\omega_\beta^2 M_{\xi_2\beta}\\0&0&\omega_\beta^2\end{bmatrix},\tilde{\boldsymbol{B}}=\begin{Bmatrix}k_\beta\omega_\beta^2 M_{\xi_1\beta}\\k_\beta\omega_\beta^2 M_{\xi_2\beta}\\k_\beta\omega_\beta^2\end{Bmatrix},\begin{Bmatrix}M_{\xi_1\beta}\\M_{\xi_2\beta}\end{Bmatrix}=\boldsymbol{\phi}^T\begin{Bmatrix}S_\beta\\S_{\alpha\beta}\end{Bmatrix}. \tag{22}$$

Once the aeroservoelastic mathematical model is constructed, the response of the BACT wing can be numerically computed via an integration algorithm [17].

Numerical Simulations and Discussions

This section presents the numerical validation of the accuracy of the parallel ROM and the robustness and anti-interference of the active flutter suppression system. The basic information required for training the ROM was computed first via a Reynolds-averaged Navier-Stokes flow solver. The specific heat ratio and Reynolds number were set to 1.132 and 3.96 million, respectively, based on the wing chord in all the computations. In the study, the Mach numbers in the numerical simulation covered a wide range, and the results of the numerical computation were given only for Mach 0.825. The ROM output and control effect data of the remaining Mach numbers are presented in a single graph as a summary.

As well known, the Filtered Gaussian White Noise (FGWN) function [18] can reduce the computation time and motivate most characteristics of nonlinear aerodynamics. In this study, therefore, the FGWN function was used as the input signal for CFD simulation. To cover the natural frequency of the BACT wing, the bandwidth of the input signal was taken as $0\sim300$ rad/s, and the amplitude of the generalized displacement of the first two orders was set as 0.2, whereas the deflection angle of control surface was assumed to be less than 5°. The time step in the CFD simulation was approximately taken as 1.0×10^{-3}s. A total of 6000 time steps were computed, and the number of input and output signals was set to 6000.

In the study, the order of the front linear part, the rear linear part and the number of neurons were taken as 8, 8, and 10, respectively. Fig.3 shows the comparison between the generalized aerodynamic forces computed via the CFD and ROM, and the input were the same FGWN signals. Fig.3 indicates that the results computed via the ROM and CFD look almost the same. These results show that the ROM could accurately predict the generalized aerodynamic forces under the above condition. To validate the accuracy of the parallel ROM when the input signals were different types, a simulation was made when the input of control surface was a sinusoidal signal. As shown in Fig.4, the output computed via the parallel ROM was in a good agreement with that via the direct CFD simulation.

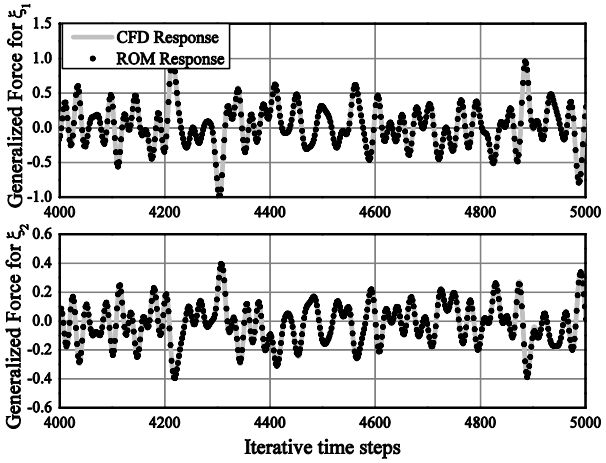

Fig.3 CFD model and parallel ROM outputs under the FWGN excitation

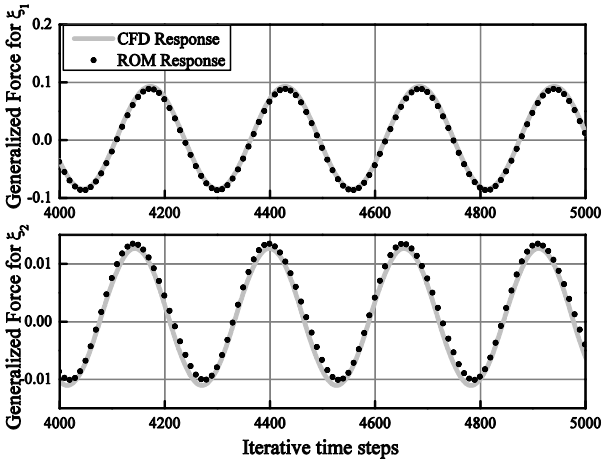

Fig.4 CFD model and parallel ROM outputs under the sinusoidal excitation

The transonic flutter boundary was first investigated in the open-loop aeroservoelastic responses of the BACT wing. To verify the precision and wide applicability of the ROM, Fig.5 presents the transonic flutter boundary predicted by the ROM in comparison with the CFD results at Ma =0.63, 0.70, 0.71, 0.75, 0.77, 0.80, 0.82, and 0.825. Moreover, Fig.5 also shows the results of parallel ROM of the Wiener type and linear ROM for comparison. As shown in the figure, the flutter boundary predicted by the parallel ROM was very close to that computed by the CFD, and had higher accuracy than that of the parallel ROM of Wiener type. Hence, the parallel ROM had high accuracy to simulate the nonlinear aerodynamic forces.

The LCO phenomenon produced due to the nonlinear aerodynamic forces is the other important research hotspot. In this study, the LCO of the BACT wing was then investigated at Ma =0.825 with q_∞ =190 psf. Fig.6 shows the time-varying generalized displacement computed via the ROM. The figure indicates that the maximum of the generalized displacement increased slowly over time, and then the maximum of the generalized displacement approached to a fixed value after a period of time. To reduce the computational time, the initial speed of the generalized model was set to $\dot{\xi}_1(0)=0$ and $\dot{\xi}_2(0)=1.5$ in the study. Fig.7 presents the comparison between the LCO computed by using the ROM of Wiener-Hammerstein type and that computed by using the CFD simulation and the ROM of Wiener type. Here, the ROM results were basically the same as the CFD results. Table 1 shows the computation times for the ROM of Wiener-Hammerstein type with training and for CFD, respectively. When the ROM was established with all parameters determined, the computation time for simulating the LCO phenomenon was only dozens of seconds. The comparison hence shows that the ROM enables one to greatly improve computation efficiency.

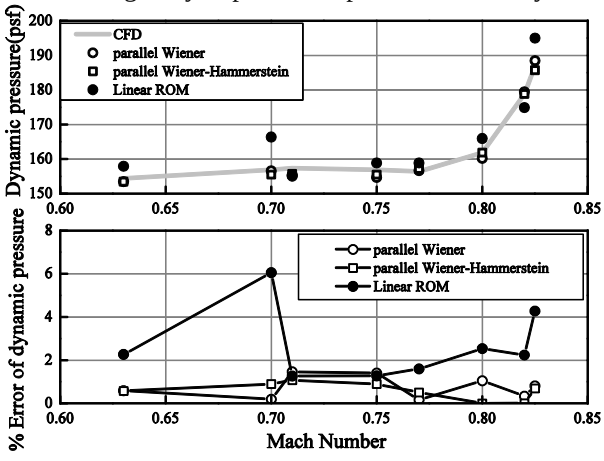

Fig.5 Comparison of the flutter dynamic pressures predicted via different models

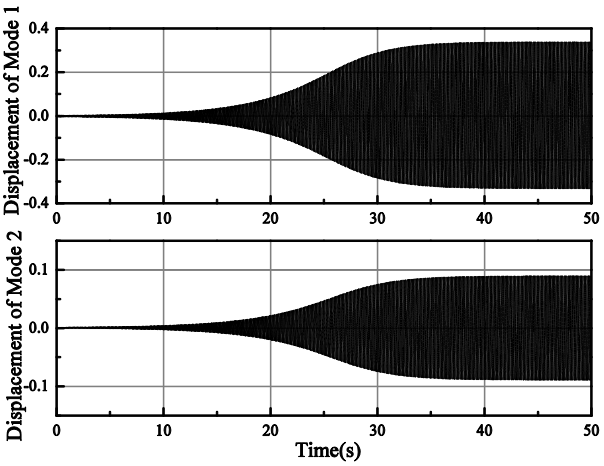

Fig.6 Time histories of LCO computed via the nonlinear parallel ROM

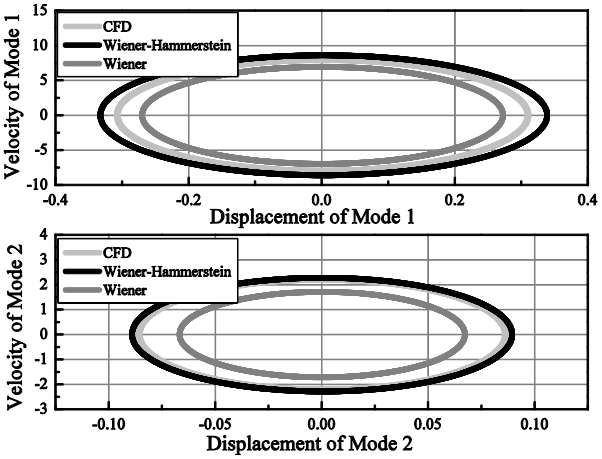

Fig.7 Comparison of the phase portraits of the LCO via different models

According to the above numerical computations, it can be concluded that the parallel ROM of Wiener-Hammerstein type can greatly shorten the computation time on the premise of guaranteeing the computation accuracy of the nonlinear aerodynamic forces. The identified ROM can completely replace CFD simulation as the control object in the design of the active flutter suppression for numerical computations.

5. Conclusions

In this study, the parallel ROM of Wiener-Hammerstein type was established and the presented ROM had a strong ability to describe nonlinear aerodynamic forces. In addition, it could precisely predict the dynamic pressure of flutter and the LCO amplitude of the three-dimensional BACT model.

References

[1] Rozza, G., 2014. Reduced Order Methods for Modeling and Computational Reduction. Springer, New York.
[2] Thomas, J.P., Dowell, E.H., Hall, K.C., 2003. Three-dimensional transonic aeroelasticity using proper orthogonal decomposition-based reduced-order models. Journal of Aircraft, 40(3), 544-551.
[3] Xie, D., Xu, M., Dowell, E.H., 2014. Proper orthogonal decomposition reduced-order model for nonlinear aeroelastic oscillations. AIAA Journal, 52(2), 229-241.
[4] Liu, H. J., Hu, H. Y., Zhao, Y. H., 2014. Efficient reduced-order modeling of unsteady aerodynamics robust to flight parameter variations. Journal of Fluids and Structures, 49, 728-741.
[5] Timme, S., Marques, S., Badcock, K.J., 2011. Transonic aeroelastic stability analysis using a kriging-based schur complement formulation. AIAA Journal, 49(6), 1202-1213.
[6] Mannarino, A., Mantegazza, P., 2014. Nonlinear aeroelastic reduced order modeling by recurrent neural networks. Journal of Fluids and Structures, 48, 103-121.
[7] Huang, R., Hu, H. Y., Zhao, Y. H., 2012a. Single-input/single-output adaptive flutter suppression of a three- dimensional aeroelastic system. Journal of Guidance, Control, and Dynamics, 35(2), 659-665.
[8] Huang, R., Li, H. K., Hu, H. Y., 2015. Open/Closed-Loop Aeroservoelastic Predictions via Nonlinear, Reduced-Order Aerodynamic Models. AIAA Journal, 53(7), 1812-1824.
[9] Huang, R., Hu, H. Y., Zhao, Y. H., 2014. Nonlinear Reduced-Order Modeling for Multiple-Input/Multiple-Output Aerodynamic Systems. AIAA Journal, 52(6), 1219-1231.
[10] Chiuso, A., 2007. The role of vector autoregressive modeling in predictor-based subspace identification. Automatica, 43(6), 1034-1048.
[11] Chiuso, A., Picci, G., 2005. Consistency analysis of some closed-loop subspace identification methods. Automatica, 41(3), 377-391.
[12] Houtzager, I., Van Wingerden, J.W., Verhaegen, M., 2012. Recursive predictor-based subspace identification with application to the real-time closed-loop tracking of flutter. IEEE Transactions on Control Systems Technology, 20(4), 934-949.

[13] Moré J.J., 1978. The Levenberg-Marquardt algorithm, implementation and theory//Numerical analysis. Springer, Berlin Heidelberg, 105-116.
[14] Scott, R.C., Hoadley, S.T., Wieseman, C.D., 2000. Benchmark active controls technology model aerodynamic data. Journal of Guidance, Control, and Dynamics, 23(5), 914-921.
[15] Kelkar, A.G., Joshi, S.M., 2000. Passivity-based robust control with application to benchmark active controls technology wing. Journal of Guidance, Control, and Dynamics, 23(5), 938-947.
[16] Waszak, M.R., 1996. Modeling the benchmark active control technology wind-tunnel model for application to flutter suppression. AIAA Paper, 1996-3437.
[17] Edwards, J.W., Bennett, R.M., Whitlow, W., 1983. Time-marching transonic flutter solutions including angle-of-attack effects. Journal of Aircraft, 20(11), 899-906.
[18] Raveh, D.E., 2004. Identification of computational-fluid-dynamics based unsteady aerodynamic models for aeroelastic analysis. Journal of Aircraft, 41(3), 620-632.